Magnetic properties and crystal field splitting of the rare-earth pyrochlore $Er_2Ir_2O_7$

Kristina Vlášková,[1] Petr Proschek,[1] Martin Diviš,[1] Duc Le,[2] Ross Harvey Colman,[1] and Milan Klicpera[1,*]

[1]*Charles University, Faculty of Mathematics and Physics, Department of Condensed Matter Physics, Ke Karlovu 5, 121 16 Prague 2, Czech Republic*

[2]*ISIS Facility, Rutherford Appleton Laboratory, Chilton, Didcot, Oxon OX11 0QX, England, United Kingdom*

(Received 10 April 2020; accepted 15 June 2020; published 21 August 2020)

The effects on the rare-earth crystal-field-splitting schemes of incorporation of large spin-orbit coupling (5*d*) ions, such as Ir^{4+}, into the rare-earth pyrochlores are largely unknown. We report on the preparation, specific heat, magnetization, and inelastic neutron-scattering study of $Er_2Ir_2O_7$ pyrochlore. An anomaly in specific heat and bifurcation of zero-field cooled and field cooled magnetization indicates an ordering of the Ir sublattice below 140 K, in good agreement with other rare-earth pyrochlore iridates. The Er sublattice ordering below 2 K can be considered short range as well, following the development of specific-heat and magnetization data down to low temperatures. The inelastic neutron scattering allowed us to unambiguously determine the crystal-field (CF) eigenenergies and parameters of $Er_2Ir_2O_7$, which are dictated dominantly by nearest-neighbor anions (the oxygen cage around the Er cation). The influence of the magnetic iridium cations on the erbium CF scheme is rather moderate despite the strong spin-orbit coupling expected in a 5*d* metal, which is evident when comparing the energy spectra of this iridate and other 3*d*- or 4*d*-metal containing erbium pyrochlores. The determined CF parameters were subsequently utilized for calculations of magnetization and specific-heat CF contributions, leading to an excellent agreement with experimental data.

DOI: 10.1103/PhysRevB.102.054428

I. INTRODUCTION

$Er_2Ir_2O_7$ belongs to the family of complex $A_2B_2O_7$ oxides (A = rare-earth element; $B = d$ or p element) crystallizing in the pyrochlore structure ($Fd\bar{3}m$, no. 227). The geometrically frustrated magnetic moments on the A and/or B lattice site, together with mutual strengths of electron correlations and spin-orbit coupling (SOC), lead to diverse magnetic ground states. Beside the long-range magnetic ordering of magnetic moments observed in Heisenberg magnet $Gd_2Sn_2O_7$ [1], the dynamical nature of magnetic ordering in $Tb_2Sn_2O_7$ [2], or the XY anisotropy order in $Er_2Ti_2O_7$ [3], also more exotic states have been reported. The prime example is the so-called spin ice state, where the spins of magnetic moments are arranged analogously to hydrogen ions in water ice, with two spins pointing in and two pointing out of their respective tetrahedra [4]. The geometrical frustration or competing spin interactions can cause also the freezing of spins and spin-glass [5] or spin liquid states, i.e., the system with distinct dynamics of correlated nonordered spins fluctuating down to the lowest temperature [6]. The magnetic Ir^{4+} ions on the B site play a crucial role—influencing the rare-earth magnetism—in formation of (especially) low-temperature properties of $A_2B_2O_7$. On the whole, spin correlations, a strong entanglement of spin and orbital degrees of freedom of its 5*d* electrons, and a comparable strength of electron Coulomb repulsion and SOC [7] make pyrochlore iridates attractive for both theoretical and experimental studies.

Beside the above-mentioned complex low-temperature states, pyrochlore iridates exhibit highly interesting electronic properties, connected to the iridium sublattice, also at higher temperatures (>100 K). The iridium sublattice is supposed to order magnetically with the all-in–all-out (AIAO) long-range structure (between 30 and 140 K, depending on the A ion, no ordering observed for the Pr analog) [7]. Such ordering is supported by magnetization measurements [a bifurcation of zero-field cooled (ZFC) and field cooled (FC) magnetization curves] [8–10], local muon spin-resonance technique [11–13], or neutron-diffraction experiments [14]. However, short-range correlations between Ir^{4+} magnetic moments, rather than their long-range ordering, have also been proposed [15–17] to explain the experimental data, particulary due to low magnetic moment on Ir. The short-/long-range magnetic ordering of the Ir sublattice is often discussed also with respect to the change of conducting properties. Metallic (A = Pr, Nd) or semimetallic/nonmetallic (A = heavier rare-earth element) $A_2Ir_2O_7$ becomes an insulator at (similar) temperature, below which the Ir^{4+} ions start to be correlated [8]. No structural transition related to magnetic ordering was observed; the pyrochlore structure is preserved down to the lowest temperature (see, e.g., Refs. [16,18]).

Magnetic moments on the rare-earth sublattice are supposed to order (depending on A) at much lower temperature, being exposed to the iridium exchange field [9,12]. The coupling between rather itinerant 5*d* Ir moments and highly localized rare-earth moments is rather weak at higher temperature. Such assumptions were, nevertheless, confuted in the case of $Tb_2Ir_2O_7$ [19], where both sublattices order antiferromagnetically already at high temperature, showing a strong interaction between Tb and Ir moments. Yet, another magnetic

*Mi.Klicpera@seznam.cz

contribution was followed below 10 K. The low-temperature magnetic behavior of the rare-earth sublattice remains enigmatic for many $A_2Ir_2O_7$, partly because of a nonstraightforward preparation of these oxides and the lack of single-crystal studies, especially on heavy rare-earth $A_2Ir_2O_7$. Furthermore, the powerful techniques of neutron scattering are limited by the large neutron absorption cross section of iridium.

Physical properties of several light rare-earth $A_2Ir_2O_7$ with small Ising moments on the A site were studied thoroughly, while few results have been published on the heavy A counterparts (see below). The polycrystalline and single-crystalline studies showed metallic behavior of $Pr_2Ir_2O_7$ down to low temperature, where a spin liquid state emerges [20,21]. A well-isolated doublet with Ising-like magnetic moments aligned along local ⟨111⟩ directions was reported [22]. The metal to insulator transition (MIT) below $T_{MIT} \sim 30$ K (depending on the sample preparation route) and the AIAO ordering of Ir moments were revealed in $Nd_2Ir_2O_7$ [23]. Further, due to the coupling between d and f electrons, the AIAO ordering is induced also on the Nd^{3+} sublattice [12,24]. The MIT and AIAO orderings of iridium moments were reported also for $Eu_2Ir_2O_7$ showing a continuous transition from paramagnetic metal to antiferromagnetic insulator [11,25]. Although the large moments of the heavy A counterparts are not supposed to be consistent with the quantum spin ice/liquid phenomena, their interactions with Ir moments lead frequently to surprising physical properties as well. Unfortunately, only a limited number of studies, typically based on data obtained employing a limited number of experimental techniques, have been published. $Tb_2Ir_2O_7$ with both Tb and Ir sublattices ordering magnetically below $T_{MIT} = 125$ K [19] serves as a prime example. The magnetic ordering of Ir and Dy is unknown in the case of $Dy_2Ir_2O_7$, which nevertheless shows unusual spin dynamics revealed by the evolution of ac susceptibility with frequency below $T_{MIT} = 135$ K [26]. Highly interesting low-temperature properties were reported for spin ice $Ho_2Ir_2O_7$, namely, the fragmentation of magnetic moment under the influence of a local staggered field [27]. AIAO ordering of the Ir sublattice and glassy freezing of Er^{3+} moments at low temperatures were suggested for $Er_2Ir_2O_7$ [9]. Concluding our short list, the investigation of $Lu_2Ir_2O_7$ with nonmagnetic Lu^{3+} brought information on magnetic properties of the Ir sublattice not influenced by rare-earth magnetism, suggesting short-range correlations rather than long-range ordering of iridium moments [10,15].

In the present paper we focus on the crystal-field (CF) excitations in $Er_2Ir_2O_7$. Although the rare-earth $A_2Ir_2O_7$ pyrochlores stand in the foreground of scientific interest, demonstrated by a number of high-impact publications, to our best knowledge no report on their single-ion excitations, to be precise on the CF, has been presented. The knowledge of the CF is, however, essential to correctly understand the physical properties of the compound as well as its ground state. Our paper leads to unambiguous determination of the CF scheme in $Er_2Ir_2O_7$. We highlight that the determined scheme is similar to the CF model of the Pt analog, as well as other investigated $Er_2B_2O_7$ pyrochlores [28]. The Ir magnetic sublattice plays a rather moderate role on the erbium CF scheme, which is actually not surprising considering highly localized $4f$ electrons and their small overlap with Ir d orbitals. Instead the

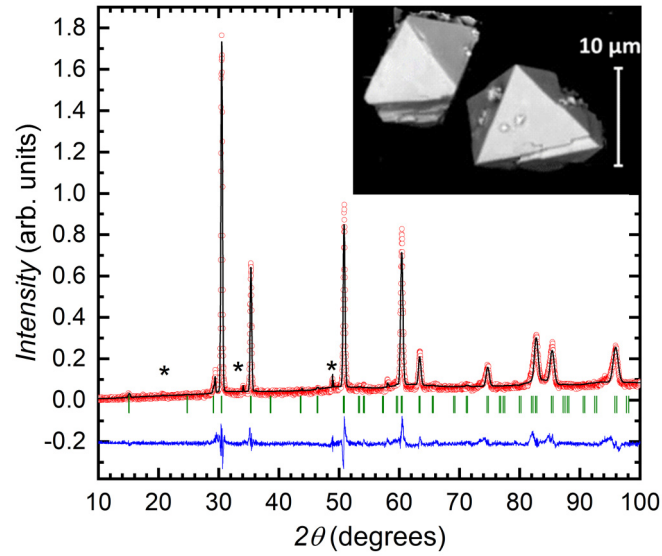

FIG. 1. The powder x-ray-diffraction patterns of $Er_2Ir_2O_7$ synthesized by the flux growth with CsCl used as a flux. Bragg peaks of the pyrochlore lattice are denoted by green bars, whereas the reflections coming from the Er_2O_3 phase are labeled with asterisks. The inset contains the BSE picture of prepared material.

CF acting on Er is predominantly determined by the nearest-neighbor oxygen anions. The determined CF eigenenergies and parameters were used to describe our specific-heat and magnetization data leading to an excellent agreement between experiment and CF calculations. Furthermore, our new bulk data (utilizing also our previous results on $Lu_2Ir_2O_7$ [15]) allowed us to identify the temperature of Ir the magnetic (short- or long-range) ordering/MIT transition, $T_{MIT} = 140$ K. The low-temperature data then strongly suggest a short-range order among Er cations below $T_{LT} = 2$ K.

II. EXPERIMENTAL METHODS AND CALCULATION DETAILS

The polycrystalline sample of $Er_2Ir_2O_7$ was prepared by flux method using initial oxides Er_2O_3 (99.99%, AlfaAesar) and IrO_2 (99.99%), and CsCl (99.999%) as a flux. The starting chemicals were heated under active vacuum up to 500 K to desorb moisture prior the weighing. The oxides with $Er_2O_3 : IrO_2 = 1 : 2$ ratio were thoroughly mixed with the CsCl in the 1 : 50 ratio, inserted into the platinum crucible, and reacted at 1073 K for seven days with intermediate grindings. Further details on sample preparation can be found elsewhere [29].

The reacted powder was investigated employing x-ray diffraction (Bruker D8-Advance with CuKα radiation) and electron microscopy [electron scanning microscope (MIRA, Tescan) with back-scattered-electron (BSE) and energy dispersive x-ray (EDX) detectors]. The diffraction patterns (Fig. 1) indicated cubic structure of prepared $Er_2Ir_2O_7$ with traces of unreacted initial oxides. The small amount of unreacted oxides is a common problem preparing $A_2Ir_2O_7$ materials. It originates from a large difference of melting temperatures of A_2O_3 and IrO_2 as well as from heavy sublimation of latter oxide at temperature significantly lower than melting

temperature. The heavy evaporation of iridium dioxide can be alleviated just by the use of the flux method, where the initial oxides are dissolved in the flux and the reaction temperature is lower, preventing the evaporation of the IrO_2. The quality of previously studied pyrochlore materials was commented upon (briefly) in most of the related publications. The flux method and whole preparation process allowed us to prepare material with less than 3% of unreacted oxides. To remove initial oxide and Pt in the $Gd_2Pt_2O_7$ sample, the boiling aqua regia was used by Hallas *et al.* [30]. We also observed a certain improvement of sample quality introducing the acids, however the minority phases remained in the studied sample. We believe that further optimization of the method is possible and eventually could lead to single phase samples. The presence of those oxides was not manifested in any of the further measured data (see further text). The evaluation of measured data was performed employing the Rietveld method and FULLPROF suite [31]. The crystal structure was confirmed to be of a pyrochlore type ($Fd\bar{3}m$) with lattice parameter $a = 10.162(1)$ Å and the fraction coordinate of the oxygen atom $x_{O\text{-}48f} = 0.334(2)$, in agreement with previously published results [9]. Despite low sensitivity of EDX to light elements (oxygen), the analysis of energy spectra of the prepared sample allowed us to confirm the Er : Ir ratio to be $50(\pm2) : 50(\pm2)$. The pyrochlore type of crystal structure was documented by a typical bipyramid form of prepared $Er_2Ir_2O_7$ crystals (of μm size) (see the BSE picture in the inset of Fig. 1).

The sample synthesized in the form of powder was pressed into the pellets for further bulk properties measurements. Magnetization measurement in temperature range 1.8–330.0 K was performed on a $\approx$ 5-mg sample employing a superconducting quantum interference device magnetometer (magnetic property measurement system, Quantum Design), while a low-temperature magnetization (0.4–7.0 K, $\approx$ 1 mg sample) was measured indirectly using a physical property measurement system (PPMS), Quantum Design, equipped with the ^{3}He option and precalibrated Hall probes. The principle of the magnetization measurement using Hall probes can be found elsewhere [32,33]. Specific heat was measured employing a standard time-relaxation method and PPMS: The low-temperature part of data (< 15 K) was collected on a $\approx$1-mg sample, while for higher temperatures the sample of $\approx$10 mg was used.

The inelastic neutron-scattering experiment was performed on the time-of-flight spectrometer MARI at the Rutherford Appleton Laboratory (ISIS), Didcot. The experiment was conducted on a 6.5-g sample with incident neutron energies, E_i, of 10, 30, 120, and 180 meV at temperatures 5, 60, 100, and 200 K. The sample was packed in aluminum foil, in an annular geometry, and placed inside an aluminum cylindrical sample holder with a diameter of 4 cm (data accessible online, see Ref. [34]). Auxiliary measurements of an empty container and vanadium for calibration purposes were performed. Data were corrected for container scattering, absorption and self-shielding, detector efficiency variation, and energy dependence. The normalization to a vanadium standard allowed the calculation of the dynamic structure factor $S(Q, \omega)$ in absolute units, employing the software package MANTIDPLOT [35].

To calculate the magnetization as a function of magnetic field, dc magnetic susceptibility, and specific heat as a function of temperature we employed the microscopic Hamiltonian, containing the trigonal crystal-field term [see Eq. (1)] and the Zeeman term. The wave functions and eigenenergies of the Er ($J = 15/2$) in CF were determined diagonalizing the model Hamiltonian. These were used to compute desired quantities using our in house computer codes [36]. The real diagonal matrix of the total angular momentum $\hat{J}_z$ operator and real symmetric matrix of the off-diagonal $\hat{J}_x$ operator were both transformed by similarity transformation $\hat{J}_z^t = Q^T * \hat{J}_z * Q$ and $\hat{J}_x^t = Q^T * \hat{J}_x * Q$, respectively. The matrix Q contained the eigenvectors of the microscopic Hamiltonian in columns and Q^T was the transpose matrix of Q. The magnetization as a function of magnetic field and temperature was obtained as $M_\parallel = g\mathrm{Tr}(\hat{J}_z^t * \rho)$, $M_\perp = g\mathrm{Tr}(\hat{J}_x^t * \rho)$ (g is the Landé factor of the ground-state multiplet). ρ is the diagonal density matrix with exponentials $e^{(-\frac{E_i}{k_B T})}$ on the main diagonal (k_B is the Boltzmann constant).

III. RESULTS AND DISCUSSION

A. Specific heat

Specific heat of $Er_2Ir_2O_7$ is characterized by low- and high-temperature anomalies [see Figs. 2(b) and 3]. A high-temperature anomaly is observed at around 140 K and can be ascribed to both MIT transition and magnetic ordering of Ir^{4+} moments, as previously reported also for other $A_2Ir_2O_7$ [7,8]. We note that such an anomaly in specific heat was not observed previously, at least on heavy rare-earth pyrochlores, except our recent study on $Lu_2Ir_2O_7$ [15]. (Such observation might point to the high quality of our sample.) The specific-heat anomaly in Lu analog data [Fig. 2(b)] is more pronounced and narrower than in the case of erbium iridate, suggesting rather continuous character of the MIT/magnetic transition in $Er_2Ir_2O_7$, possibly caused by interaction between Ir and Er ions (the Lu^{3+} ion is supposed to be nonmagnetic). The temperature, at which the specific-heat anomaly is observed, is well consistent with our magnetization data—bifurcation of ZFC and FC data [see Fig. 2(a) and Sec. III B]. Assuming the anomaly is connected to magnetic contribution of the iridium sublattice to specific heat, we estimated its entropy to be $S_{Ir} = 0.38$ J K^{-1} mol^{-1}. In order to do so, the high-temperature specific-heat data were fitted by a smooth curve and subtracted from total specific heat, in the same way as previously done for $Lu_2Ir_2O_7$ [15]. Comparing the calculated entropies of both analogs, the lutetium iridate ($S_{Ir} = 0.57$ J K^{-1} mol^{-1}) anomaly is connected with slightly higher entropy. Both values are consistent with the entropy reported for $Nd_2Ir_2O_7$ (0.47 J K^{-1} mol^{-1}) and somewhat lower than entropy of $Sm_2Ir_2O_7$ (2.00 J K^{-1} mol^{-1}) and $Eu_2Ir_2O_7$ (1.40 J K^{-1} mol^{-1}) anomalies [8], and simultaneously much lower than $R\ln(2) = 5.7$ J K^{-1} mol^{-1}, where R is the universal gas constant. Such small values were discussed in the context of frustration of magnetic moments or itinerancy of 5d electrons. Furthermore, the influence of lattice and electronic contributions to specific heat cannot be fully ruled out by simple subtraction. In contrast, assuming the anomaly is connected to MIT, we can estimate electronic specific-heat coefficient [8]

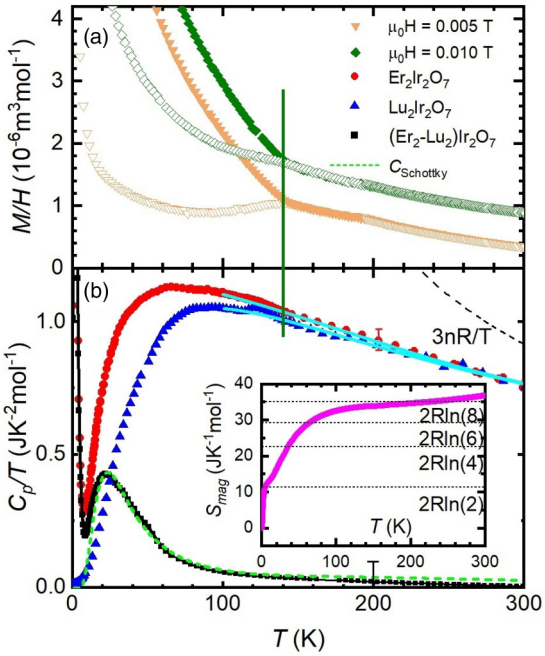

FIG. 2. The high-temperature (a) magnetization and (b) specific heat of $Er_2Ir_2O_7$. The empty (full) symbols in panel (a) stand for the magnetization measured under the ZFC (FC) condition. Panel (b) contains the total specific heat C_p of $Er_2Ir_2O_7$, its nonmagnetic counterpart $Lu_2Ir_2O_7$, and their difference. The high-temperature part of C_p's is approximated by the solid lines in order to subtract the anomalies from data (see text for details). The Schottky contribution to specific heat based on CF energy levels is shown by the dashed line. The vertical line within both panels marks the temperature of ZFC-FC bifurcation (T_{MIT}) and simultaneously the onset of the specific-heat anomaly. The inset shows the upper limit of magnetic entropy calculated based on the difference between $Er_2Ir_2O_7$ and $Lu_2Ir_2O_7$ data.

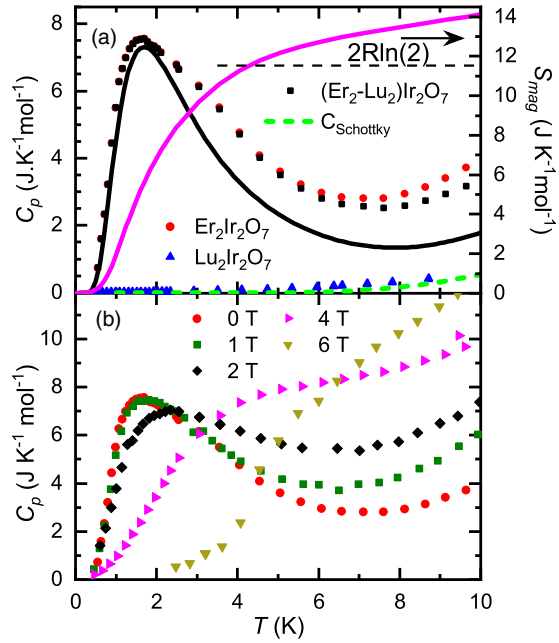

FIG. 3. (a) The low-temperature part of the specific heat of $Er_2Ir_2O_7$, its nonmagnetic counterpart $Lu_2Ir_2O_7$, and their difference $(Er_2\text{-}Lu_2)Ir_2O_7$. The corresponding magnetic entropy, S_{mag} (purple line, right axis), is presented as well. The Schottky contribution to specific heat calculated from CEF energies is shown by the green dashed line. The black line represents the simulation of exchange interaction modeled by an internal field of 0.9 T splitting the ground-state doublet (see text for details). (b) The field development of the low-temperature anomaly of $Er_2Ir_2O_7$.

$\gamma_{MIT} = S_{Ir}/T_{MIT} = 2.7$ mJ K^{-2} mol^{-1}, where $T_{MIT} = 140$ K. A similar value of $\gamma_{MIT} = 4.1$ mJ K^{-2} mol^{-1} was estimated for $Lu_2Ir_2O_7$ [15] pointing to semimetallic character of the iridate.

Low-temperature specific heat is dominated by the $T_{LT} = 2$ K anomaly of magnetic origin. The lattice and electronic contributions to specific heat are well approximated by the $Lu_2Ir_2O_7$ analog as presented in Fig. 3(a). The magnetic entropy reaches the value of Rln(2) at 4.5 K, coinciding with the onset of the specific-heat anomaly, and suggesting the splitting of the Er^{3+} ground-state doublet due to magnetic correlations among erbium moments. Generally, the anomaly could be ascribed also to a low-energy CF excitation. Such a scenario is, however, unambiguously ruled out by our inelastic neutron-scattering experiment (see Sec. III C). The anomaly becomes broader and shifts to higher temperature in applied magnetic field [Fig. 3(b)]. Such a field evolution of specific heat would be consistent with long-range ferromagnetic ordering; the magnetic correlations among magnetic moments become stronger in applied field. However, considering the shape of the anomaly and negative Curie-Weiss (CW) temperature, the antiferromagnetic short-range correlations (a spin-glass-like state) should be considered instead. To estimate the effect of exchange interactions on the ground-state CF doublet, a simple model (see Sec. II) was used. The splitting of the Er^{3+} doublet and with it connected specific heat were calculated considering the magnetic field of the order of tesla (ranging from 0.5 to 2.0 T). The best agreement with measured data was obtained considering the internal field of 0.9 T [see black line in Fig. 3(a)]. The low-temperature part of the anomaly was well described, while the specific heat at higher temperature showed larger values than our crude model. Although the agreement is reasonable, the magnetic exchange interactions at low temperatures should be considered more complex; further the magnetic interactions between Er and Ir sublattices cannot be ruled out.

The erbium magnetic contribution to specific heat, C_{mag}, on the whole temperature interval was calculated subtracting the data of the $Lu_2Ir_2O_7$ analog from $Er_2Ir_2O_7$. First, the high-temperature anomaly was subtracted from the data, for both Er and Lu analogs, to roughly remove the magnetic contribution of Ir moments [see Fig. 2(b) with smoothed data above 100 K]. We note that the estimated C_{mag} (as well as S_{mag}) represents the upper limit of the magnetic contribution to specific heat. Except for the low-temperature anomaly at T_{LT}, C_{mag} exhibits a pronounced anomaly at 25 K and rather broad anomaly around 170 K. At high temperature, the values of specific heat of both analogs are large and similar, leading to significant scatter of the data and large error bars [for better lucidity, only one error bar for each data set is shown at 200 K in Fig. 2(b)].

The high-temperature anomalies in C_{mag} are generally ascribed to changes in the internal energy of the system, Schottky specific heat. The ground-state multiplet of Kramers's Er^{3+} ion ($J = 15/2$) splits in crystal electric field into doublets and quadruplets, depending on point-group symmetry of the atomic position it occupies. As the Wyckoff position of erbium in the $Fd\bar{3}m$ space group is $16c$, the point symmetry is not cubic (leading to some levels being four times degenerated), but trigonal (D_{3d}, $-3m$). Therefore, the energy spectrum of $Er_2Ir_2O_7$ contains eight CF doublets, where one doublet is the ground state. Both observed high-temperature anomalies are well described by the Schottky contribution to the specific heat [dashed line in Fig. 2(b)] calculated from CF excitation energies, as determined by inelastic neutron spectrocsopy (INS) experiment (Sec. III C).

Inspecting the magnetic entropy shown in the inset of Fig. 2(b), we observe four regions: (i) the low-temperature region, where the entropy rises from zero to the value of $R\ln(2)$ with increasing temperature, corresponding to splitting of the ground-state doublet due to magnetic correlations; (ii) the region below 90 K, where the entropy increases significantly up to $R\ln(6)$, demonstrating that the first two excitations/doublets have not significantly different energies, both lower than ≈ 9 meV; (iii) the region below 220 K, with entropy developing almost linearly with temperature up to $R\ln(8)$, pointing to the third excited doublet at energy < 20 meV; and finally (iv) the high-temperature region (> 220 K), exhibiting further entropy increase, presumably up to the value of $R\ln(16)$ at significantly higher temperature; four CF doublets are expected in the higher-energy region. Our analysis of magnetic entropy is fully consistent with INS data presented in Sec. III C.

B. Magnetization

The high-temperature magnetization data are well described by the CW law. No differences were observed on M/H data comparing the measurements with applied magnetic field of 0.5, 5.0, and 7.0 T (see Fig. 4). A linear evolution of inverse dc susceptibility is followed down to 50 K, showing no sign of anomaly at around T_{MIT} connected to the magnetic correlations between iridium ions. The fitted effective magnetic moment of $\mu_{eff} = 9.12\ \mu_B$ is sufficiently close to the moment expected for the free Er^{3+} ion ($\mu_{eff} = 9.58\ \mu_B$). CW temperature of $\theta_p = -26$ K points to antiferromagnetic correlations in $Er_2Ir_2O_7$. We note that the high-temperature magnetic behavior of the compound is strongly influenced/dominated by the erbium sublattice. Such a fact is not surprising considering different magnetic moments of respective ions. The fit of the Lu analog data to CW [15] led to values of $\mu_{eff} = 0.88\ \mu_B$ and $\theta_p = -217$ K, respectively. Such a conclusion is further supported by a good agreement of the high-temperature magnetization data and calculated magnetic susceptibilities based on CF parameters (no exchange interactions were taken into account)—the INS data were analyzed considering only the erbium sublattice (see Sec. III C).

Investigating the magnetization data in detail, a bifurcation of zero-field cooled and field cooled magnetization in small external magnetic field [of 0.005 and 0.010 T; see Fig. 2(a)] is followed. The temperature of the bifurcation coincides with the onset of the specific-heat anomaly in Fig. 2(b) (a vertical line in the figure is provided to guide the reader). Such a bifurcation was observed already in previous study on $Er_2Ir_2O_7$ [9]—as well as for other compounds from the $A_2Ir_2O_7$ family [7]—and was ascribed to both (long-range) magnetic ordering of the iridium sublattice and MIT. Our recent study on $Lu_2Ir_2O_7$, with Lu^{3+} being nonmagnetic, confirmed the bifurcation origins in the Ir correlations [15]. Comparing the data measured on Er and Lu analogs (as well as $A_2Ir_2O_7$ with A = Sm-Yb [7]), especially the values of transition temperatures, the differences are small, pointing to rather weak interactions between the Er (A) and Ir sublattices at high temperature. So far, $Tb_2Ir_2O_7$ is the sole example of a heavy rare-earth $A_2Ir_2O_7$ oxide showing strong coupling between the two sublattices at high temperature—as indicated by magnetization and neutron-diffraction data [9,19].

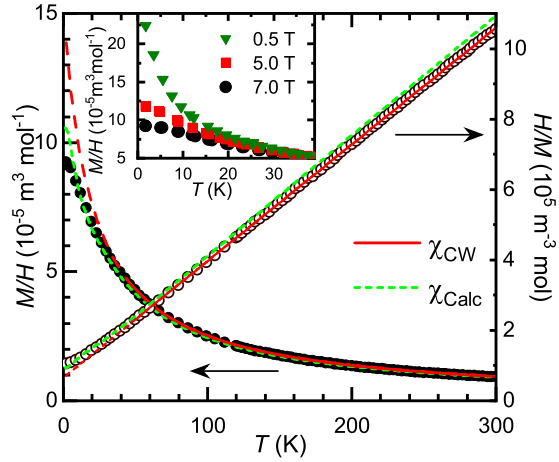

FIG. 4. DC magnetic susceptibility and its inverse value measured in an external magnetic field of 7 T. The full red line represents the Curie-Weiss fit of susceptibility and it is extrapolated as the dashed line down to low temperature. The dashed green line stands for magnetic susceptibility calculated from CF parameters in Table I. The inset contains the low-temperature region of the figure showing also the magnetization measured in other high magnetic fields.

The magnetic correlations among rare-earth ions become stronger at lower temperature leading to a strong dependence of magnetization on applied magnetic field below 40 K and hence to a deviation from CW behavior (inset of Fig. 4). The magnetization $M/H(T)$ develops strongly (decreases) with applied field from 0.005 to 7.000 T at low temperature, whereas only subtle field dependence is observed in the high-temperature region. The magnetic correlations between erbium ions are further documented by isothermal magnetization data in Fig. 5, exhibiting properties consistent with either antiferromagnetic or short-range order. The magnetization increases with increasing field and tends to saturate in high magnetic field (not saturated in 7 T). The value of magnetization in 7 T exceeds the value expected for the Er^{3+} free ion ($9\ \mu_B$) within the mean-field approximation and is likely to further increase in higher magnetic field. The larger value of magnetization can be explained by an additional contribution originating in the magnetic moment of Ir^{4+}, having the value of $1.74\ \mu_B$ for $S = 1/2$. Nevertheless, comparing

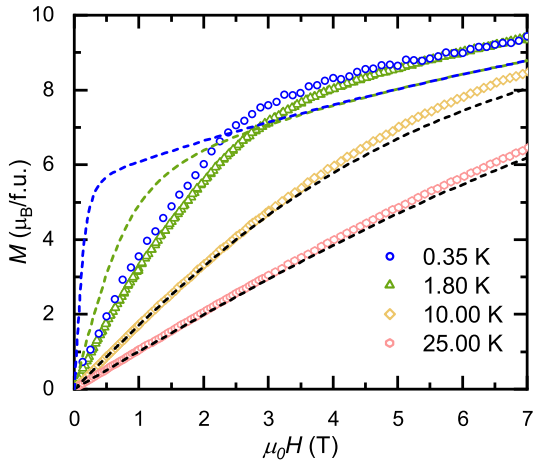

FIG. 5. The isothermal magnetization of $Er_2Ir_2O_7$. The dashed lines represent the respective magnetization calculated from CF parameters in Table I.

the measured data with the magnetization calculated from CF parameters (INS experiment data analyzed in Sec. III C), a very similar development in high magnetic field is followed on both. The difference between measured and calculated curves is narrowing with increasing field (Fig. 5). According to expectations, the CF-based calculations better coincide with magnetization data measured at higher temperatures (> 2 K), i.e., at temperatures where the magnetic correlations between erbium moments are weak.

C. Inelastic neutron scattering

The inelastic neutron-scattering experiment performed on the powder sample employing the MARI spectrometer disclosed an energy spectrum of $Er_2Ir_2O_7$, more accurately the magnetic (CF) excitations scheme, and its development with momentum transfer [$Q = |(\vec{Q})|$] and temperature.

Inspecting the measured data in Fig. 6, several energy regions with magnetic signal are identified. The signal corresponding to three transitions between ground state and respective excited states is found at around 5.5, 9, and 20 meV. Much broader magnetic signal is seen between 60 and 75 meV. Finally, a weak magnetic signal is traced at 90 meV. No magnetic excitation is observed at higher energy up to 150 meV. A magnetic origin of the observed signal is unambiguously proven by its Q dependence: The signal becomes weaker with increasing Q following well the Q dependence of the magnetic form factor. An example of the Q development of intensity of the first three excitations is shown in Fig. 7. The inset of Fig. 7 presents a comparison between Q dependence of magnetic form factor $F^2(Q)$ and measured intensity of the first CF excitation. The same Q dependence was followed for all excitations.

The magnetic origin of observed excitations is further documented by the temperature evolution of measured intensity. To follow the intensity evolution, the measured data were analyzed constructing so-called Q cuts by integration of the signal in the low-Q region (Fig. 8). The intensity of magnetic (CF) excitations decreases with increasing temperature due to substantial thermal population of individual energy levels. Further, thermally populated energy levels allow the neutron to gain energy, leading to both (de-)excitations in the neutron-energy-gain (system-energy-loss) part of the spectrum and excitations between excited states. Such excitations are clearly observed in spectra measured at 60, 100, and 200 K (Fig. 8). Let us illustrate the influence of thermal population of energy levels in the low-energy part of the spectrum [focusing on the excitation at 5.5 meV in Fig. 8(a)]: The excited state is mostly unpopulated at 5 K—the temperature (i.e., thermal energy; $E = k_B T$, where k_B is the Boltzmann constant) is too small to noticeably populate the energy states, therefore the measured spectrum contains signal only in the neutron-energy-loss part. By increasing the temperature up to 60 K, the energy levels become partially thermally occupied. The excitation in the neutron-energy-gain part of spectrum is observed in -5.5 meV. Further signal is pronounced at 3.5 meV corresponding to the excitation from the 5.5-meV state to the 9-meV state. A respective excitation takes place (at -3.5 meV) in the neutron-energy-gain part of the spectrum. Additional increase of temperature leads to further thermal population of energy states, i.e., to a decrease of intensity of the "base-temperature" excitation at 5.5 meV and increase of intensity of "temperature-induced" excitations (-5.5, -3.5, and 3.5 meV). A high-enough temperature causes all states

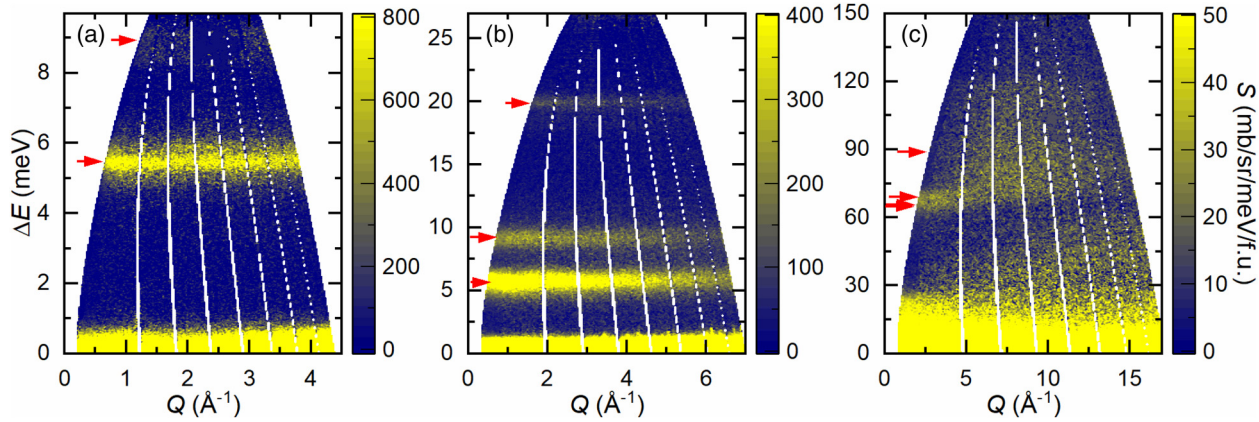

FIG. 6. The EQ maps measured with incident energies (a) 10 meV, (b) 30 meV, and (c) 180 meV at 5 K. The arrows mark the CF excitations.

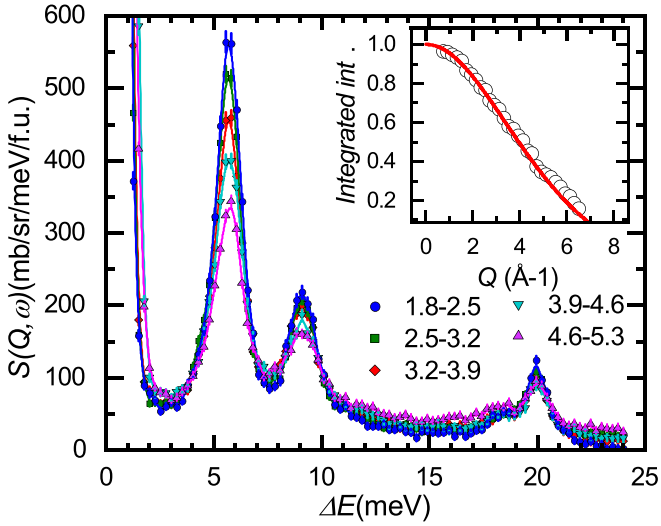

FIG. 7. Q cuts of the map measured with $E_i = 30$ meV, representing the development of excitation intensity with increasing Q. The inset compares the Q dependence of the integrated intensity of the first excitation and magnetic form factor of Er^{3+} (tabulated value taken from Ref. [37]).

to be (partly) thermally populated and all types of (de-)excitations to be manifested.

The CEF excitations in $Er_2Ir_2O_7$ are well described within a standard crystal-field model. Er^{3+} ions ($J = 15/2$) occupy Wyckoff position (16c in the $Fd\bar{3}m$ space group) with a trigonal point symmetry (D_{3d}, $-3m$). Therefore the crystal-field Hamiltonian can be written as follows:

$$\hat{H}_{\mathrm{CEF}} = B_2^0\hat{O}_2^0 + B_4^0\hat{O}_4^0 + B_4^3\hat{O}_4^3 + B_6^0\hat{O}_6^0 + B_6^3\hat{O}_6^3 + B_6^6\hat{O}_6^6. \quad (1)$$

B_n^m are the crystal-field parameters and O_n^m stand for Steven's operators representing the erbium $4f$ shell. The model implies a splitting of the Er^{3+} 16-times ($= 2J + 1$) degenerate ground-state multiplet in CEF into eight doublets protected by Kramers's theorem. Seven transitions from the ground state are expected in the base-temperature energy spectrum of $Er_2Ir_2O_7$.

To identify all seven expected CF transitions in the energy spectra is not necessarily straightforward, which is also the case for $Er_2Ir_2O_7$, where a previous investigation identified only four of the seven excitations required to fully fit and characterize the crystal-field scheme [38]. Although the number of excitations was low, the CF parameters for $Er_2Ir_2O_7$ were determined in previous study. However, to unambiguously identify the CF scheme and parameters all seven excitations have to be accounted for. Three low-energy excitations are clearly observed; the shape of the peaks in Fig. 8 excludes that they could individually consist of more than one contribution. The region between 60 and 75 meV contains at least two magnetic peaks, one at 65 meV and a second at 69 meV. The peak at 90 meV is relatively broad and of weak intensity. Therefore, one cannot be conclusive that it corresponds to a single excitation. Counting the peaks, one excitation is still missing to reveal a complete expected spectrum for $Er_2Ir_2O_7$. The missing signal was eventually found within the 65-meV

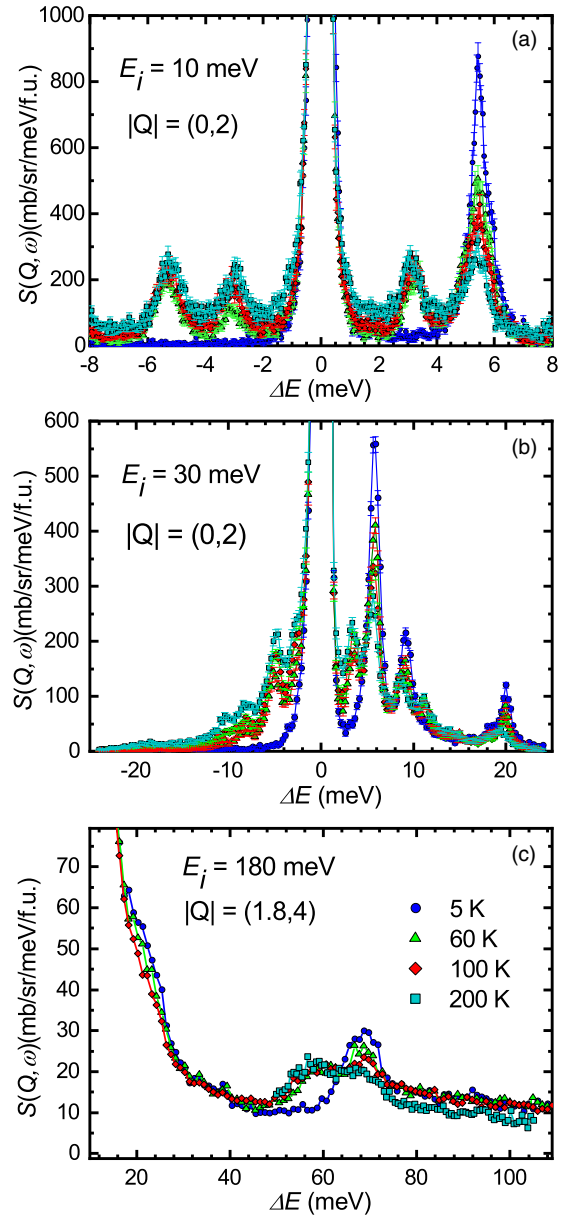

FIG. 8. Q cuts of EQ maps measured at various listed temperatures, demonstrating a thermal population of the energy states with increasing temperature.

peak, which consists of two contributions. The two peaks close to each other (64.84 and 65.57 meV) cannot be unambiguously distinguished in our data [Fig. 8(c), including the data measured with 120 meV of incident energy, not shown] due to resolution limitations. However, all the fitting of the region between 60 and 75 meV by three peaks (peak positions were restricted to lie within the interval and to have similar intensities), previous results on other Er-based pyrochlores [28], and our fit of the data to the CF model (consistent with magnetic susceptibility data) confirm such a scenario. The excitation energies obtained by fitting the individual peaks by a Lorentzian function are listed in Table I and are graphically represented by arrows in Fig. 6.

We note a striking resemblance of the energy scheme of $Er_2Ir_2O_7$ to other Er-based pyrochlores, especially $Er_2Pt_2O_7$

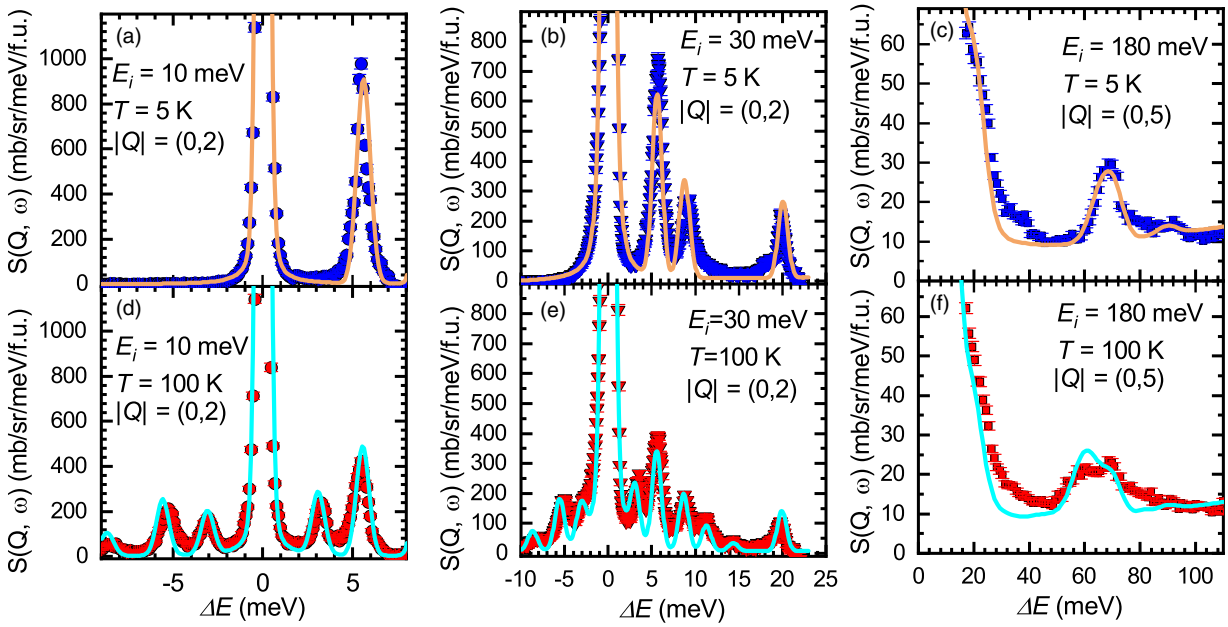

FIG. 9. Q cuts of EQ maps measured at 5 and 100 K. The solid lines represent the fit to the CEF Hamiltonian [Eq. (1)] resulting in CF energies and parameters listed in Table I.

[28]. The magnetic Ir^{4+} ions have, somewhat surprisingly, a negligible effect on the CF scheme of Er^{3+} in $Er_2Ir_2O_7$. Comparing the energy schemes of the analogs with different magnetic and nonmagnetic d or p elements on the B site, and their similarity, the following conclusion can be drawn. The CF acting on Er^{3+} is predominantly determined by nearest-neighbor O^{2-} anions forming the cubic cage around it. The substitution of the element on the B site leads to the change of crystallographic parameters, i.e., change of dimensions/shape of the oxygen octahedra, which results in the (only slightly) different CF scheme. The atomic radii of Ir and Pt differ negligibly, which is consistent with very similar crystallographic parameters [a = 10.162(1) and 10.13(2) Å [28] and x_{O48f} = 0.334(2) and 0.340 [28], respectively] of the two $Er_2B_2O_7$ analogs, as well as with their similar CEF schemes.

The measured data were fitted to the model CF Hamiltonian [Eq. (1)] utilizing the previously reported CF parameters for $Er_2Pt_2O_7$ [28] as starting values. First, the fit of 5-K data—combining three energy spectra measured with initial neutron energies 10, 30, and 180 meV—was done leading to the CF energies and parameters listed in Table I. Subsequently, these parameters were used as starting values to fit the data measured at all temperatures (i.e., 5, 60, 100, and 200 K). We remind the reader that at elevated temperature the intensity of individual excitations changes and simultaneously new excitations, corresponding to transitions between thermally populated energy levels, occur. The fitted spectra are presented in Fig. 9 and the values of final CF energies and parameters are listed in Table I. Small differences between parameters obtained by fitting the 5-K spectra only and parameters refined fitting the spectra at all temperatures demonstrate a good quality of initial fit as well as the consistency of our experimental data measured at different temperatures.

Refined CF energies were used to calculate the Schottky contribution to the specific heat and compared to the experimental data in Fig. 2(b). Calculated specific heat (dashed line) corresponds well to C_{mag} data (black squares), perfectly reproducing the two observed anomalies. The CEF scheme is also fully consistent with the temperature evolution of magnetic entropy [inset of Fig. 2(b)] as discussed above. The first three CF excitations (the temperature of specific-heat measurement was limited) are followed on both the change of slope of the entropy curve and the entropy value at temperatures corresponding to the CF energies ($E = k_BT$).

The magnetic susceptibility calculated from CF parameters is well in agreement with measured data in Fig. 4. The susceptibility was calculated for two local crystallographic directions: along (z) and perpendicular to ($\perp$) the local (tetragon) ⟨111⟩ axes. The measured data reveal values remarkably close to the susceptibility calculated for the perpendicular component. Calculating a powder average of these susceptibilities by a simple formula, $\chi_{powder} = \frac{1}{3}(\chi_z + 2\chi_\perp)$, leads to a very good agreement with the experimental data (Fig. 4). A good agreement between isothermal magnetization data and calculations based on CF parameters is followed in Fig. 5, especially for higher temperature, i.e., sufficiently above T_{LT}.

The magnetic anisotropy is well characterized by respective g tensors $g_\perp$ and g_z and their ratio. Calculated values of g's are listed in Table I. Although the $g_\perp > g_z$ was reported for all previously investigated $Er_2B_2O_7$ [28], their ratio differs substantially depending on the B ion. For light elements B = Ti and Ge, the $g_\perp/g_z$ was determined to be of an order of magnitude smaller than for the heavier B = Sn and Pt. Different magnetic structures of previously investigated erbium pyrochlores [28] likely arise just from different strengths of XY anisotropy. Our results on the Ir analog do not fully fit to the $Er_2B_2O_7$ systematics, suggesting the low-temperature structure to be of Γ_5 manifold [28,39,40]. A somewhat larger value of $g_\perp/g_z$ still consistent with Γ_5 was reported earlier [38]. However, neither our data (including the elastic part of Fig. 6, containing the peaks corresponding to the nuclear

TABLE I. Experimental parameters determined investigating $Er_2Ir_2O_7$: content of Er:Ir in the prepared sample, lattice parameter a, fraction coordinate $x_{O\text{-}48f}$, low- and high-temperature anomaly temperature T_{LT} and T_{MIT}, gamma coefficient γ_{MIT} and entropy S_{Ir} attributed to the MIT and Ir sublattice, effective magnetic moment μ_{eff} and paramagnetic Curie-Weiss temperature θ_p, CF eigenenergies E_i and parameters B_n^m, and g tensors $g_\perp$ and g_z and their ratio. The wave functions of the ground-state doublet $|\phi_0\pm\rangle$, see text for details.

Parameter	Value
Er:Ir	50(±2):50(±2)
a (Å)	10.162(1)
$x_{O\text{-}48f}$	0.334(2)
T_{LT} (K)	2
T_{MIT} (K)	140
γ_{MIT} (mJ K^{-2} mol^{-1})	2.7
S_{Ir} (J K^{-1} mol^{-1})	0.38
μ_{eff} (μ_B)	9.12(2)
θ_p (K)	−26(2)
Parameter	Experiment
E_0 (meV)	0
E_1 (meV)	5.652(1)
E_2 (meV)	9.221(1)
E_3 (meV)	19.859(2)
E_4 (meV)	64.841(4)
E_5 (meV)	65.568(4)
E_6 (meV)	68.913(5)
E_7 (meV)	88.782(9)
Parameter	Fit of 5-K data
E_0 (meV)	0
E_1 (meV)	5.628(2)
E_2 (meV)	8.761(2)
E_3 (meV)	20.060(3)
E_4 (meV)	64.109(4)
E_5 (meV)	65.433(4)
E_6 (meV)	70.339(5)
E_7 (meV)	89.735(8)
B_2^0 (10^{-2} meV)	7.478(2)
B_4^0 (10^{-3} meV)	1.868(2)
B_4^3 (10^{-2} meV)	1.152(3)
B_6^0 (10^{-6} meV)	9.753(2)
B_6^3 (10^{-4} meV)	−1.488(5)
B_6^6 (10^{-4} meV)	2.422(5)
Parameter	Final CEF fit
E_0 (meV)	0
E_1 (meV)	5.581(2)
E_2 (meV)	8.684(2)
E_3 (meV)	19.937(2)
E_4 (meV)	64.149(4)
E_5 (meV)	65.391(4)
E_6 (meV)	70.214(6)
E_7 (meV)	89.935(8)
B_2^0 (10^{-2} meV)	7.456(1)
B_4^0 (10^{-3} meV)	1.886(2)
B_4^3 (10^{-2} meV)	1.148(2)
B_6^0 (10^{-6} meV)	9.720(3)
B_6^3 (10^{-4} meV)	−1.473(3)
B_6^6 (10^{-4} meV)	2.418(3)
Parameter	Value
$g_\perp$	6.275(2)
g_z	3.043(2)
$g_\perp/g_z$	2.206(1)

reflections of pyrochlore structure) nor data presented in Ref. [9] allowed us to be conclusive on magnetic ordering in $Er_2B_2O_7$. Instead, a short-range correlation/freezing of the Er^{3+} magnetic moments was followed down to the lowest temperature.

IV. CONCLUSIONS

The crystal field in $A_2Ir_2O_7$—in our case A = Er—has been fully described. The inelastic neutron-scattering experiment on $Er_2Ir_2O_7$ allowed us to unambiguously determine the CF eigenenergies and parameters, which are similar to other $Er_2B_2O_7$, especially for B = Pt. We conclude that the effect of the magnetic iridium cations on the erbium CF scheme is rather weak. Instead, the oxygen cubic cage around Er determines the CF acting on it. The specific-heat and magnetization data measured on $Er_2Ir_2O_7$ are well in agreement with calculation based on determined CF parameters. Furthermore, the anomaly in specific heat and bifurcation of ZFC and FC magnetization identified the (short- or long-range) ordering temperature of the Ir sublattice to be 140 K, well in line with other rare-earth pyrochlore iridates. Concurrently, the low-temperature data suggest short-range correlations among Er moments below 2 K, rather than long-range magnetic ordering observed in other $Er_2B_2O_7$ pyrochlores.

ACKNOWLEDGMENTS

This work was supported by the Czech science foundation under Grant No. 18-09375Y. The work of K.V. was further supported by GAUK Project No. 558218. The preparation, characterization, and measurement of bulk physical properties on $Er_2Ir_2O_7$ were performed in MGML [41], which was supported within the program of Czech Research Infrastructures (Project No. LM2018096). We gratefully acknowledge the Science and Technology Facilities Council for access to neutron beamtime at ISIS, MARI facility.

[1] A. S. Wills, M. E. Zhitomirsky, B. Canals, J. P. Sanchez, P. Bonvill, P. Dalmas de Reotier, and A. Yaouanc, Magnetic ordering in $Gd_2Sn_2O_7$: The archetypal Heisenberg pyrochlore antiferromagnet, J. Phys.: Condens. Matter **18**, L37 (2006).

[2] I. Mirebeau, A. Apetrei, J. Rodríguez-Carvajal, P. Bonville, A. Forget, D. Colson, V. Glazkov, J. P. Sanchez, O. Isnard, and E. Suard, Ordered Spin Ice State and Magnetic Fluctuations in $Tb_2Sn_2O_7$, Phys. Rev. Lett. **94**, 246402 (2005).

[3] A. Poole, A. S. Wills, and E. Levièvre-Berna, Magnetic ordering in the XY pyrochlore antiferromagnet $Er_2Ti_2O_7$: A spherical neutron polarimetry study, J. Phys.: Condens. Matter **19**, 452201 (2007).

[4] S. T. Bramwell and M. J. P. Gingras, Spin ice state in frustrated magnetic pyrochlore materials, Science **294**, 1495 (2001).

[5] K. Binder and A. P. Young, Spin glasses: Experimental facts, theoretical concepts and open questions, Rev. Mod. Phys. **58**, 801 (1986).

[6] J. S. Gardner, S. R. Dunsiger, B. D. Gaulin, M. J. P. Gingras, J. E. Greedan, R. F. Kiefl, M. D. Lumsden, W. A. MacFarlane, N. P. Raju, J. E. Sonier, I. Swainson, and Z. Tun, Cooperative Paramagnetism in the Geometrically Frustrated Pyrochlore Antiferromagnet $Tb_2Ti_2O_7$, Phys. Rev. Lett. **82**, 1012 (1999).

[7] W. Witzak-Krempa, G. Chen, Y. B. Kim, and L. Balents, Correlated quantum phenomena in the strong spin-orbit regime, Annu. Rev. Condens. Matter Phys. **5**, 57 (2014).

[8] K. Matsuhira, M. Wakeshima, Y. Hinatsu, and S. Takagi, Metal-insulator transitions in pyrochlore oxides $Ln_2Ir_2O_7$, J. Phys. Soc. Jpn. **80**, 094701 (2011).

[9] E. Lefrancois, V. Simonet, R. Ballou, E. Lhotel, A. Hadj-Azzem, S. Kodjikijan, P. Lejay, P. Manuel, D. Khalyavin, and L. Chapon, Anisotropy-Tuned Magnetic Order in Pyrochlore Iridates, Phys. Rev. Lett. **114**, 247202 (2015).

[10] N. Taira, M. Wakeshima, and Y. Hinatsu, Magnetic properties of iridium pyrochlores $R_2Ir_2O_7$ (R = Y, Sm, Eu and Lu), J. Phys.: Condens. Matter. **13**, 5527 (2001).

[11] S. Zhao, J. M. Mackie, D. E. MacLaughlin, O. O. Bernal, J. J. Ishikawa, Y. Ohta, and S. Nakatsuji, Magnetic transition, long-range order, and moment fluctuations in the pyrochlore iridate $Eu_2Ir_2O_7$, Phys. Rev. B **83**, 180402(R) (2011).

[12] H. Guo, K. Matsuhira, I. Kawasaki, M. Wakeshima, Y. Hinatsu, I. Watanabe, and Zhu-an Xu, Magnetic order in the pyrochlore iridate $Nd_2Ir_2O_7$ probed by muon spin relaxation, Phys. Rev. B **88**, 060411(R) (2013).

[13] S. M. Disseler, Ch. Dhital, A. Amato, S. R. Giblin, C. de la Cruz, S. D. Wilson, and M. J. Graf, Magnetic order in the pyrochlore iridates $A_2Ir_2O_7$ (A = Y, Yb), Phys. Rev. B **86**, 014428 (2012).

[14] H. Guo, C. Ritter, and A. C. Komarek, Direct determination of the spin structure of $Nd_2Ir_2O_7$ by means of neutron diffraction, Phys. Rev. B **94**, 161102(R) (2016).

[15] M. Klicpera, K. Vlášková, and M. Diviš, Low-temperature properties of pyrochlore $Lu_2Ir_2O_7$, J. Magn. Magn. Mater. **506**, 166793 (2020).

[16] M. C. Shapiro, S. C. Riggs, M. B. Stone, C. R. de la Cruz, S. Chi, A. A. Podlesnyak, and I. R. Fisher, Structure and magnetic properties of the pyrochlore iridate $Y_2Ir_2O_7$, Phys. Rev. B **85**, 214434 (2012).

[17] S. M. Disseler, S. R. Giblin, Ch. Dhital, K. C. Lukas, S. D. Wilson, and M. J. Graf, Magnetization and Hall effect studies on the pyrochlore iridate $Nd_2Ir_2O_7$, Phys. Rev. B **87**, 060403 (2013).

[18] J. P. Clancy, H. Gretarsson, E. K. H. Lee, Di Tian, J. Kim, M. H. Upton, D. Casa, T. Gog, Z. Islam, B.-G. Jeon, K. H. Kim, S. Desgreniers, Y. B. Kim, S. J. Julian, and Y.-J. Kim, X-ray scattering study of pyrochlore iridates: Crystal structure, electronic, and magnetic excitations, Phys. Rev. B **94**, 024408 (2016).

[19] H. Guo, C. Ritter, and A. C. Komarek, Magnetic structure of $Tb_2Ir_2O_7$ determined by powder neutron diffraction, Phys. Rev. B **96**, 144415 (2017).

[20] S. Nakatsuji, Y. Machida, Y. Maeno, T. Tayama, T. Sakakibara, J. van Duijn, L. Balicas, J. N. Millican, R. T. Macaluso, and Julia Y. Chan, Metallic Spin-Liquid Behavior of the Geometrically Frustrated Kondo Lattice $Pr_2Ir_2O_7$, Phys. Rev. Lett. **96**, 087204 (2006).

[21] Y. Tokiwa, J. J. Ishikawa, S. Nakatsuji, and P. Gegenwart, Quantum criticality in a metallic spin liquid, Nat. Mater. **13**, 356 (2014).

[22] Y. Machida, S. Nakatsuji, H. Tonomura, T. Tayama, T. Sakakibara, J. van Duijn, C. Broholm, and Y. Maeno, Crystalline electric field levels and magnetic properties of the metallic pyrochlore compound $Pr_2Ir_2O_7$, J. Phys. Chem. Sol. **66**, 1435 (2005).

[23] S. M. Disseler, Direct evidence for the all-in/all-out magnetic structure in the pyrochlore iridates from muon spin relaxation, Phys. Rev. B **89**, 140413 (2014).

[24] Z. Tian, Y. Kohama, T. Tomita, H. Ishizuka, T. H. Hsieh, J. J. Ishikawa, K. Kindo, L. Balents, and S. Nakatsuji, Field-induced quantum metal-insulator transition in the pyrochlore iridate $Nd_2Ir_2O_7$, Nat. Phys. **12**, 134 (2015).

[25] J. J. Ishikawa, E. C. O'Farrell, and S. Nakatsuji, Continuous transition between antiferromagnetic insulator and paramagnetic metal in the pyrochlore iridate $Eu_2Ir_2O_7$, Phys. Rev. B **85**, 245109 (2012).

[26] K. Matsuhira, M. Wakeshima, Y. Hinatsu, Ch. Sekine, C. Paulsen, T. Sakakibara, and S. Takagi, Slow dynamics of Dy pyrochlore oxides $Dy_2Sn_2O_7$ and $Dy_2Ir_2O_7$, J. Phys.: Conf. Ser. **320**, 012050 (2011).

[27] E. Lefrancois, V. Cathelin, E. Lhotel, J. Robert, P. Lejay, C. V. Colin, B. Canals, F. Damay, J. Ollivier, B. Fak, L. C. Chapon, R. Ballou, V. Simonet *et al.*, Fragmentation in spin ice from magnetic charge injection, Nat. Commun. **8**, 1 (2017).

[28] J. Gaudet, A. M. Hallas, A. I. Kolesnikov, and B. D. Gaulin, Effect of chemical pressure on the crystal electric field states of erbium pyrochlore magnets, Phys. Rev. B **97**, 024415 (2018).

[29] K. Vlášková, R. H. Colman, and M. Klicpera, The synthesis and characterisation of the $Er_2Ir_2O_7$ pyrochlore (unpublished).

[30] A. M. Hallas, A. Z. Sharma, Y. Cai, T. J. Munsie, M. N. Wilson, M. Tachibana, C. R. Wiebe, and G. M. Luke, Relief of frustration in the Heisenberg pyrochlore antiferromagnet $Gd_2Pt_2O_7$, Phys. Rev. B **94**, 134417 (2016).

[31] J. Rodrìguez-Carvajal, Recent advances in magnetic structure determination by neutron powder diffraction, Physica B: Condensed Matter **192**, 55 (1993).

[32] A. Candini and M. Affronte, Magnetometry by means of Hall microprobes in the Quantum Design PPMS (2008), https://qdusa.com/siteDocs/appNotes/1084-701.pdf.

[33] K. Vlášková, R. H. Colman, P. Proschek, J. Čapek, and M. Klicpera, Evidence for spin-glass ground-state in defect-fluorite $Er_2Zr_2O_7$ single crystals, Phys. Rev. B **100**, 214405 (2019).

[34] M. Klicpera *et al.*, Magnetic excitations in $A_2Ir_2O_7$, STFC ISIS Facility (2019), doi:10.5286/ISIS.E.RB1920419.

[35] J. Taylor, O. Arnold, J. Bilheaux, A. Buts, S. Campbell, M. Doucet, N. Draper, and R. Fowler, MANTID: A high performance framework for reduction and analysis of neutron scattering data, Bull. Am. Phys. Soc. **57** (2012).

[36] G. J. Bowden, D. P. Bunbury, and M. A. H. McCausland, Crystal fields and magnetic anisotropy in the molecular field approximation. I: General considerations, J. Phys. C **4**, 1840 (1971).

[37] A. J. Freeman and J. P. Desclaux, Dirac-Fock studies of some electronic properties of rare-earth ions, J. Magn. Magn. Mater. **12**, 11 (1979).

[38] E. Lefrancois, Synthesis and study of iridium oxide compounds for entangled spin-orbit physics, Ph.D. thesis, Université Grenoble Alpes, 2006.

[39] A. Bertin, Y. Chapuis, P. D. de Reotier, and A. Yaouanc, Crystal electric field in the $R_2Ti_2O_7$ pyrochlore compounds, J. Phys.: Condens. Matter **24**, 256003 (2012).

[40] A. M. Hallas, J. Gaudet, and B. D. Gaulin, Experimental insights into ground-state selection of quantum XY pyrochlores, Ann. Rev. Condens. Matter Phys. **9**, 105 (2018).

[41] See http://mgml.eu/.